Braz J Phys (2015) 45:673–686
DOI 10.1007/s13538-015-0351-x

SOCIEDADE BRASILEIRA DE FÍSICA

NUCLEAR PHYSICS

Elastic and Inelastic α-Scatterings from ^{58}Ni, ^{116}Sn, and ^{208}Pb Targets at 288, 340, 480, and 699 MeV

Kassem O. Behairy[1] · **Zakaria M. M. Mahmoud**[2,3] · **M. A. Hassanain**[2,4]

Received: 26 June 2015 / Published online: 9 September 2015

Abstract Real double-folding optical potentials are calculated using the *S1Y* effective nucleon-nucleon (*NN*) interaction and the *tρρ* approximation in order to analyze elastic and inelastic scattering of α-particles from ^{58}Ni, ^{116}Sn, and ^{208}Pb targets at 288, 340, 480, and 699 MeV. The relativistic corrections for momenta and reduced masses are performed to investigate the data at the energies 480 and 699 MeV. The second-order (double-scattering) correction to the *tρρ* potential is also considered. The inelastic scattering to low-lying excited states (2^+) is investigated using the distorted wave born approximation (DWBA) and the coupled-channel (CC) techniques.

Keywords Optical potential · Double folding · Elastic and inelastic α-nucleus scattering · tρρ approximation · Coupled channels

1 Introduction

Intermediate and high-energy α-particle scatterings are a useful tool for studying the heavy ion (HI) interaction. The α-particle scattering is proven also to be a sensitive tool for studying the nuclear matter distributions and the transition densities of nuclei since the α-particle is a very symmetric nucleus with a simple structure. The elastic scattering of α-particles at high enough energies (E_α>100 MeV) resolves the discrete ambiguities of the optical potential that occur in the analyses of data at lower energies [1, 2]. In addition, inelastic α-particle scattering is a valuable tool for studying both low-lying states and giant resonances. While low-lying states are studied extensively at lower beam energies (under 60 MeV), higher energies are required to investigate the isoscalar giant resonances [3].

The scattering of α-particles projectile from light heavy ion targets is of special interest because elastic scattering cross sections exhibit two different features. The first is usually known as anomalous large angle scattering (ALAS) [4], where an unusual enhancement of the cross section is observed at back angles. The second feature is the nuclear rainbow scattering [5], which is observed for α energies above 100 MeV. It is characterized by a sharp decrease of the cross section beyond a certain scattering angle, known as the grazing angle. These two features or phenomena can be used to probe the nucleus-nucleus potential, not only in the surface region but also at smaller distances, and could be of considerable practical use in eliminating certain potential ambiguities that arise in the analysis of elastic scattering data. The interpretation of these two features played a decisive role in establishing a unique α-nucleus optical potential [4].

Bonin et al. [6] measured and studied collisions of α-particle beams at the intermediate energies 288, 340, 480, and 699 MeV from the ^{58}Ni, ^{116}Sn, and ^{208}Pb targets. Three sets of phenomenological Woods-Saxon (WS) potential parameters were obtained from the analyses of elastic and inelastic data. Continuous ambiguities in the determination of the potentials are studied, and a possible approach is proposed to represent graphically the evolution of the optical potential as

✉ Kassem O. Behairy
drkasemomar@yahoo.com

[1] Physics Department, Aswan University, Aswan, Egypt

[2] Physics Department, Faculty of Science, Assiut University, New Valley Branch, Egypt

[3] Physics Department, Philipps University Marburg, D-35032 Marburg, Germany

[4] Physics Department, King Khalid University, Abha, Saudi Arabia

the energy varies. No discrete ambiguities are found for energies around 100 MeV, and the real part of the optical potential is a steadily decreasing function of the incident energy. A slight loss of sensitivity in the external part of the potential is observed at higher energies (480 and 699 MeV). A more recent study was done by Clark et al. [3]. They measured and analyzed the elastic and inelastic scattering of 240 MeV alpha particles on ^{58}Ni, ^{116}Sn and ^{197}Au targets and investigated the isoscalar giant resonances at intermediate energies. The energy dependence of the volume integrals of the real and imaginary potentials in the energy range 115–480 MeV is investigated.

During the last three decades, the double-folding (DF) model [7] had been widely used to generate the real parts of both the α-nucleus and HI optical potentials. The real part of the optical potential calculated using the DF model yielded a good account of α-particle scattering over a wide range of energies and target mass numbers [8, 9]. This pointed out the ability of the folding concept to predict the radial shape of the real potentials. The present work is an extension of previous studies [10–13] to test the performance of the DF optical model potentials to analyze the α-particle elastic and inelastic scattering processes at intermediate and high energies. In this work, the real DF optical potential is obtained to analyze the α-particle elastic scattering at the intermediate energies (288, 340, 480, and 699 MeV) from the ^{58}Ni, ^{116}Sn, and ^{208}Pb targets. At high and intermediate bombarding energy, a direct relationship between the nuclear densities and the optical potential is possible, as long as the effects of multiple *NN* scattering can be neglected. In the DF approach, two types of the effective interactions are used in this work. For the first choice, the effective *NN* interaction is taken to be the free *NN t*-matrix; this refers as the impulse approximation (IA) or $t\rho\rho$ approximation [14–17]. The second-order (double-scattering) correction to the $t\rho\rho$ potential is also considered. For the second choice, the *S1Y* [18] effective interaction is used.

The inelastic scattering to low-lying excited states (2^+) is investigated. Two techniques are alternatively used to interpret and analyze experimental data of direct reactions or inelastic scattering, the so-called CC (coupled channels) and DWBA (distorted wave born approximation) methods. These two methods are applied with considerable success to provide quantitative as well as qualitative information about nuclear structure and dynamics [19–21]. By CC method, we mean the solution of a relatively small set of coupled equations that results from considering a wave function model with small number of terms. This method is usually used when there is a strong coupling between the elastic and the inelastic channels. It is necessary to solve the coupled equations for the wave functions in all reaction channels to obtain the amplitude for non-elastic events. The numerical solution of the coupled equations, even in their truncated form, is however a very laborious process. In many cases, it is sufficiently accurate to use an expression for the scattering matrix element that is the limit of weak coupling between the elastic and inelastic channels. The DWBA method is the first-order solution in that weak coupling interaction for the Schrödinger equation, using the distorted wave born approximation (DWBA) and coupled channels (CC) techniques for ^{58}Ni and ^{116}Sn targets. Also, the data are analyzed in the framework of the phenomenological optical potentials.

The manuscript is organized as follows: Section 2 is for the theoretical formalism, while the procedure is explained in Section 3. Results and discussion are given in Section 4, and the general conclusions are summarized in Section 5.

2 Theoretical Formalism

2.1 The Folding Model

The real nuclear optical potential for nucleus-nucleus scattering in the DF model is usually defined by the expression

$$V^{DF}_{A_PA_T}(R)\int \rho_{Ap}(r_1)\rho_{A_T}(r_2)\upsilon_{NN}(s,E)d\vec{\boldsymbol{r}}_1 d\vec{\boldsymbol{r}}_2 \tag{1}$$

$\rho A_P(r_1)$ and $\rho_{A_T}(r_2)$ are the nuclear matter density distributions of both the projectile and target nuclei, respectively, and $\upsilon_{NN}(s,E)$ is the effective *NN* interaction, $s=\left|\vec{R}-\vec{r}_1+\vec{r}_2\right|$ is the separation distance, and E is the laboratory energy per incident nucleon. Using the Fourier transformation technique [7], this potential can be expressed in the momentum representation as

$$\begin{aligned} V^{DF}_{A_PA_T}(R) &= \sum\nolimits_{N=p,n}(2\pi)^{-3}\int e^{-iqR}\rho_{A_P}(q)\rho_{A_T}(q)\ \ \upsilon_{NN}(q)d\ \vec{q} \\ &= \frac{1}{2\pi^2}\int j_0(qr)\ \ \rho_{A_P}(q)\rho_{A_T}(q)\upsilon_{NN}(q)q^2dq \end{aligned} \tag{2}$$

Here, $j_0(qr)$ is the spherical Bessel function of zero order. The scattering from this potential at high energies (E>100 MeV/nucleon) can be calculated using the Schrodinger equation (SE) for two particles with masses M_P and M_T (the relativistically corrected masses for projectile and target), such that

$$M_P=m_P\gamma_P^{\text{c.m.}},\quad M_T=m_T\gamma_T^{\text{c.m.}}$$

where

$$\gamma_P^{\text{c.m.}}=\frac{x+\gamma_P^L}{\left(1+x^2+2x\gamma_P^L\right)^2},\quad \gamma_T^{\text{c.m.}}=\frac{\frac{1}{x}+\gamma_P^L}{\left(1+\frac{1}{x^2}+\frac{1}{2x}\gamma_P^L\right)^2},\quad \text{and } \gamma_P^L=1+\frac{E_L}{m_Pc^2}$$

$x=m_P/m_T$, and E_L is the bombarding energy in the laboratory system. With the relativistic correction, the reduced mass $\tilde{\mu}$ and the center of mass energy [22, 23] are given by

$$\tilde{\mu}=\frac{\tilde{T}}{c^2}=\frac{M_P m_T}{M_P+m_T},\quad \tilde{T}=T\frac{m_T c^2}{T+m_T c^2}$$

T is the total energy of the projectile in the c.m. system, and $\tilde{T}$ is the reduced total energy. Thus, the center of mass kinetic energy $E^{\mathrm{adj}}_{\mathrm{c.m.}}$ of the SE with these relativistic corrections is given by

$$E^{\mathrm{adj}}_{\mathrm{c.m.}}=20.901\frac{\tilde{k}^2}{\tilde{\mu}}$$

which generates the appropriate $\tilde{k}$ value,

$$\tilde{k}=\left(\frac{m_P c}{\hbar}\right)\left[\left(\gamma_P^{\mathrm{c.m.}}\right)^2-1\right]^{1/2}=4.72056 m_P\left[\left(\gamma_P^{\mathrm{c.m.}}\right)^2-1\right]^{1/2}\mathrm{fm}^{-1}$$

Thus, the standard non-relativistic optical model computer program may be used with masses M_P and m_T, and an effective bombarding energy, which is given by

$$E^{\mathrm{adj}}_{\mathrm{Lab}}=E^{\mathrm{adj}}_{\mathrm{c.m.}}\frac{M_P+m_T}{m_T} \tag{3}$$

These kinematic factors used in the non-relativistic Schrodinger-like equation are generated and listed in Table 1.

2.2 Nuclear Matter Density Distributions

As it is well known, the first important ingredient in the folding model is the nuclear density. Several forms are used [24] to represent the matter distribution of α-nucleus. In this work, we adopted two versions of these forms. The first of them that was suggested by Satchler and Love [7] in a Gaussian form as

$$\rho_\alpha(r)=0.4229\exp\left(-0.7024r^2\right) \tag{4}$$

The second expression was for Baye et al. [25]; it is also of a Gaussian form,

$$\rho_\alpha(r)=4\left(\frac{3\pi b^2}{4}\right)^{-3/2}\exp\left(-\frac{4}{3b^2}r^2\right) \tag{5}$$

with $b=1.28$ fm. For all target densities, we use the two-parameter Fermi form (FM), which is defined as

$$\rho_{A_T}(r_2)=\rho_0\left[1+\exp\left(\frac{r_2-R}{\alpha}\right)\right]^{-1} \tag{6}$$

Here, a is the diffuseness, R is the half-value radius, and $\rho_0=3/[4\pi R^3(1+(\pi^2a^2/R^2))]$. The parameters ρ_0, R, and α and the corresponding root-mean-square (rms) radius, $\langle r^2\rangle^{1/2}$, values for ^{58}Ni [26], ^{208}Pb [27], and ^{116}Sn nuclei are listed in Table 2. In terms of the rms radius $\acute{R}$ for the FM distribution we have, $R=[(5/3\acute{R})^2-(7/3)\pi^2a^2-(5/3)r_{pr}^2]^{1/2}$ where r_{pr} is the proton radius. The corresponding momentum representation of the Fermi density is approximated as

$$\rho_{A_T}(q)=\frac{8\pi\rho_0}{q^3}\,\frac{ze^{-z}}{1-e^{2z}}\left(\sin x\frac{z(1+e^{-2z})}{1-e^{-2z}}-x\cos x\right) \tag{7}$$

where $z=\pi aq$ and $x=Rq$; for more details, see ref. [28]. As an approximation, the form factor of the Fermi distribution could be represented also, [29] with precision better than 97 % for any value of r by:

$$\left[1+\exp\left(\frac{r_2-R}{a}\right)\right]^{-1}=C\left(\bar{x}\right),\quad \bar{x}=\frac{r_2-R}{a}$$
$$C\left(\bar{x}\le 0\right)=1-\frac{7}{8}e^{\bar{x}}+\frac{3}{8}e^{2\bar{x}}$$
$$C\left(\bar{x}\ge 0\right)=e^{-\bar{x}}\left(1-\frac{7}{8}e^{-\bar{x}}+\frac{3}{8}e^{-2\bar{x}}\right)$$

Table 1 The adjusted energies, wave numbers, and nuclear masses, according to the relativistic corrections

Target	E_{Lab} (MeV)	E_{adj} (MeV)	$\tilde{k}$ (MeV/c)	$M_{T\ (\mathrm{corr})}$ (amu)	$M_{P\ (\mathrm{corr})}$ (amu)
^{58}Ni	480	471.5	9.18	23.76	4.45
	699	686.6	11.2	30.95	4.65
^{208}Pb	480	464.0	9.679	36.65	4.495
	699	675.75	11.83	59.96	4.72

Table 2 Fermi form nuclear density parameters

Nucleus	ρ_0 (fm^{-3})	R (fm)	a (fm)	$\langle r^2\rangle^{1/3}$(fm)
^{58}Ni	0.154	4.094	0.54	3.7531
^{116}Sn	0.207	5.55	0.515	4.706
^{208}Pb	0.150	6.80	0.515	5.604

2.3 The Effective *NN* Interaction

The second important ingredient in the folding model is the effective *NN* interaction. For this purpose, we used two different effective *NN* interactions in the present work, namely the *S1Y* and *tρρ* effective interaction.

2.3.1 The S1Y Effective NN Interaction

The *S1Y* effective *NN* interaction has the phenomenological form [18]

$$\upsilon_{NN}(s) = (\upsilon + iw)\frac{\exp(-s/t)}{s/t} \tag{8}$$

where υ and w are, respectively, the real and imaginary strengths, s (fm) is the *NN* separation, and t (fm) is the range of the interaction.

2.3.2 The tρρ Approximation

The nucleus-nucleus *tρρ* interaction, obtained when *NN t*-matrix is inserted in the double-folding integral, would determine the energy dependence of the resulting, complex ion-ion potential [16, 17]. Thus, we write

$$V^{(1)}_{A_PAT}(r) \cong t(\theta = 0^\circ; E)\int \rho_{A_P}(r)\rho_{A_T}(r-\acute{r})d\ \vec{\acute{r}} = -4\pi\frac{E}{k^2}f_{NN}(\theta = 0^\circ; E)\int \rho_{A_P}(r)\rho_{A_T}(r-\acute{r})d\ \vec{\acute{r}} \tag{9}$$

Here, $f_{NN}(\theta)$ is the *NN* scattering amplitude. With the help of the optical theorem, we may obtain the imaginary part of $V^{(1)}_{A_PA_T}(r)$ as

$$Im\,V^{(1)}_{A_PA_T}(r) = -\frac{E}{k}\sigma_{NN}(E)\int \rho_{A_P}(r)\rho_{A_T}(r-\acute{r})d\ \vec{\acute{r}} \tag{10}$$

The real part of $V^{(1)}_{A_PA_T}(r)$ can be obtained from

$$Re\,f_{NN} = \alpha_{NN}Im\,f_{NN,} \qquad Im\,f_{NN} = \frac{k\sigma^T_{NN}}{4\pi}\exp(-\alpha_{NN}q^2) \tag{11}$$

The *NN* cross sections, σ_{NN}, as well as the parameters α_{NN} and a_{NN}, are used as input to construct the optical potential in the "*tρρ*" approximation. For energies lower than 94 MeV/nucleon, a_{NN}=0.5 fm^2 (Table 3).

For the second-order (double-scattering) contribution to the ion-ion potential, we have used the following relation:

$$V^{(1)}_{A_PA_T}(r) = -\left(\frac{ik}{4E}\right)R_{\text{corr}}\left(\int \left[V_{NA_P}(r-\acute{r})^2\right]\rho_{A_T}(\acute{r})\ d\ \vec{\acute{r}} + \iint \left[V_{NA_T}(r-\acute{r})^2\right]\ \rho_{A_P}(\acute{r})d\ \vec{\acute{r}}\right) \tag{12}$$

$V_{NA_i}(r)$ is the nucleon-nucleus (A_i,i=P,T) potential ($t\rho$). The imaginary r and real parts of the second-order nucleus-nucleus potential are

$$\begin{aligned} Re\ V^{(2)} &= -\frac{E}{2k}|R_{\text{corr}}|\alpha_{NN}\sigma_T^2\left\langle\rho^2_{A_P}\rho_{A_T} + \rho^2_{A_T}\rho_{A_{P1}}\right\rangle(r) \\ Im\ V^{(2)} &= -\frac{E}{4k}|R_{\text{corr}}|(\alpha_{NN}-1)\sigma_T^2\left\langle\rho^2_{A_P}\rho_{A_T} + \rho^2_{A_T}\rho_{A_P}\right\rangle(r) \\ \left\langle\rho^2_{A_P}\rho_{A_T} + \rho^2_{A_T}\rho_{A_P}\right\rangle(r) &= \int \rho^2_{A_P}(r-\acute{r})\rho_{A_T}(\acute{r})d\ \vec{\acute{r}} \\ &\quad + \int \rho^2_{A_T}(r-\acute{r})\rho_{A_P}(\acute{r})d\ \vec{\acute{r}} \end{aligned} \tag{13}$$

R_{corr} as presented by Hussein [17] and Ray [16] is actually composed of four distinct contributions,

$$R_{\text{corr}} = R_{\text{Pauli}} + R_{\text{SRD}} + R_{\text{PSR}} + R_{\text{CM}} \tag{14}$$

Following Boridy and Feshbach [30], R_{Pauli} is related to the Pauli exclusion-principle correlations, R_{SRD} is related to the short-range dynamical correlations, R_{PSR} is connected to the combination of the Pauli and a short-range dynamical term, and finally R_{CM} arises from the center of mass correlations. The approximate expressions for these four contributions to R_{corr} are derived [16, 17] as

Table 3 The *NN* scattering parameters

E (MeV/nucleon)	σ^T_{NN}(fm^2)	α_{NN}	α_{NN} (fm^2)
30	19.6	0.87	0.5
38	14.6	0.89	0.5
40	13.5	0.9	0.5
49	10.4	0.94	0.5
85	6.1	1.0	0.5
94	5.5	1.07	0.51
120	4.5	0.7	0.58
200	3.2	0.6	0.062

$$\left.\begin{aligned} -R_{\mathrm{Pauli}} &= -\frac{1}{2}\left(1-\frac{5}{A}+\frac{4}{A^2}\right)\frac{3\pi}{10k_F(r)}\ \ \frac{1}{1+\frac{8}{5}\overline{B}k_F^2(r)}, \\ -R_{\mathrm{SRD}} &= -\frac{1}{2}\left(1-\frac{2}{A}+\frac{1}{A^2}\right)\sqrt{\pi}\frac{b^3}{b^2+8\overline{B}}, \\ R_{\mathrm{PSR}} &= -\frac{1}{2}\left(1-\frac{5}{A}+\frac{4}{A^2}\right)\frac{3\pi}{10}\left(k_F^2(r)+\frac{5}{b^2}\right)^{-1/2}\left[1+8\overline{B}\left(\frac{k_F^2(r)}{5}+\frac{1}{b^2}\right)\right]^{-1}, \\ R_{\mathrm{CM}} &= \left(1-\frac{2}{A}+\frac{1}{A^2}\right)\ l_c. \end{aligned}\right\} \tag{15}$$

The parameters A, $k_f(r)$, $\overline{B}$, b, *and* l_c are the target mass number, local Fermi momentum, finite-range parameter of nucleon-nucleon elastic *t*-matrix, short-range dynamical correlation parameter, and the effective "correlation length", respectively.

3 Procedure

To analyze the α-particle elastic and inelastic scattering data, we use the semi-microscopic DF real potential based on *S1Y* and $t\rho\rho$ effective *NN* interactions. The imaginary parts of the α-nucleus optical potential are parameterized phenomenologically in a WS shape. The Coulomb potential is considered as the interaction of point charged projectile with spherical charged target of radius, $R_C = r_C A_T^{1/3}$; r_C is the Coulomb radius parameter, fixed at 1.3 fm in this work. Throughout this analysis, we consider the following procedures:

1) Firstly, the elastic scattering data are analyzed using the phenomenological WS potentials optimized by the auto-search computer code HI-OPTIM-94 [31]. The search is carried out on the six WS parameters. Average 10 % experimental errors, for all the considered data sets, are used through this analysis. The adjusted WS parameters are listed in Table 4.
2) Elastic scattering calculations are performed using real DF potentials based on *S1Y* effective *NN* interaction (with a fixed range at t=0.7 fm and the depth υ has been optimized in order to fit the experimental data) and then using real DF potentials based on $t\rho\rho$ effective *NN* interaction. These potentials renormalized by the factor N_R. These potential are denoted as *S1Y*(*R*) denotes for real *S1Y*-based potentials and $t\rho\rho(R)$ for real $t\rho\rho$-based potentials. Calculation based on Satchler and Love [7] density is denoted as D1, and calculations based on Baye et al. [25] is denoted as D2. The obtained best fitted parameters of elastic scattering calculation are listed in Tables 5 and 6.
3) The next stage of calculations is performed by introducing the second-order (double-scattering) correction $(t\rho(\rho)^2)$ approximation for potentials at high energies (>100 MeV).
4) Corrections to the input masses and energies are made to achieve a proper relativistic treatment using non-relativistic computer code HI-OPTIM-94 [31]. $t\rho\rho^2(R)$ denotes the real part with relativistic kinematics. The adjusted parameters are listed in Table 7.
5) Using the WS potential [32, 33] parameters for elastic scattering, DWBA calculations for low-lying (2^+) states are carried out with DWUCK4 [34]. Using the semi-microscopic potentials generated for elastic scattering, CC calculations for the same state are carried out with CHUCK3 [35] using the collective form factor.

Table 4 Phenomenological WS parameters for alpha elastic and inelastic scattering using DWBA analysis

Energy (MeV)	V_0 (MeV)	r_V (fm)	a_V (fm)	$-J_R$ (MeV fm^3)	W_0 (MeV)	r_W (fm)	a_W (fm)	$-J_I$ (MeV fm^3)	χ^2	σ_R (mb)	δ_2 (fm)	δ_2 (fm)[a]
α±^{58}Ni												
288	71.8	0.963	0.786	230.2	24.2	1.070	0.597	96.70	4.0	1462	0.82	1.09
340	65.6	0.959	0.840	213.5	26.8	1.031	0.796	103.5	2.6	1584	0.8	1.04
480	50.9	0.960	1.130	183.6	43.4	1.000	0.720	150.0	2.6	1543	0.76	1.05
699	44.8	0.960	0.820	146.0	42.3	0.870	0.990	117.0	5.0	1472	0.66	
α+^{116}Sn												
288	75.6	0.987	0.819	206.0	22.5	1.086	0.856	81.00	3.0	2289	0.71	0.81
340	74.7	1.013	0.840	220.2	24.5	1.121	0.811	94.50	2.0	2361	0.73	0.82
480	57	1.000	1.047	176.8	32.7	1.060	0.750	106.5	5.3	2138	0.69	0.85
α+^{208}Pb												
288	80.8	1.026	0.891	208.0	23.7	1.110	0.877	77.30	4.9	3087		
340	78.7	1.030	0.855	207.5	24.9	1.130	0.771	83.00	5.8	3002		
480	65.9	1.020	0.973	171.2	48.2	1.020	0.861	124.0	8.6	2977		
699	42.3	0.752	1.430	65.0	54.1	1.041	0.826	144.0	6.2	2992		

[a] From ref. [14]

Table 5 Optical potential parameters obtained using Gaussian density (D1) and Baye density (D2) from the analysis of $\alpha+^{58}$Ni scattering

Energy (MeV)	Potential	Density	v (MeV)	N_R	$-J_R$ (MeV fm^3)	W_0 (MeV)	r_W (fm)	a_W (fm)	$-J_I$ (MeV fm^3)	χ^2	σ_R (mb)
288	$S1Y(R)$	D1	33.8		144.3	5.70	1.610	0.676	74.00	4.5	2104
		D2	36.0		153.4	5.80	1.586	0.685	72.50	4.2	2063
	$t\rho\rho\,(R)$	D1		0.6	180.0	10.6	1.216	0.912	66.30	5.6	1692
		D2		0.6	171.0	9.00	1.299	0.930	68.00	5.8	1808
340	$S1Y(R)$	D1	32.3		138.0	6.80	1.633	0.788	94.00	4.6	2353
		D2	34.3		146.0	6.90	1.620	0.816	94.00	3.9	2352
	$t\rho\rho\,(R)$	D1		0.5	148.0	7.80	1.550	0.950	95.50	7.5	2357
		D2		0.5	143.4	7.40	1.590	0.880	95.50	7.0	2358
480	$S1Y(R)$	D1	32.5		139.0	10.0	1.595	0.986	134.0	4.0	2626
		D2	31.7		135.0	9.90	1.610	0.987	135.0	4.7	2652
	$t\rho\rho\,(R)$	D1		1.0	157.6	12.8	1.420	1.320	137.3	5.6	2675
		D2		1.0	157.6	14.1	1.351	1.380	137.3	6.0	2649
699	$S1Y(R)$	D1	27.9		120.2	80.4	0.864	0.850	201.2	10.0	1546
		D2	28.5		122.8	82.2	0.870	0.840	208.2	11.0	1556
	$t\rho\rho\,(R)$	D1		0.8	173.0	93.0	0.670	1.162	163.0	8.0	1651
		D2		0.8	174.0	89.0	0.685	1.156	163.6	8.6	1660

6) We confine the folding procedure to the real transition potential only. The imaginary transition potentials are obtained from the derivative of the imaginary central phenomenological potential using the deformation parameters β_L, as that in the DF real transition potential, i.e.,

$$W_{tr}(r) = -\delta_L^W \frac{dW(r)}{dr} \tag{16}$$

where $\delta_L^W = \beta_L^W r_I A_T^{1/3}$. Implicit in our calculation is the assumption that the deformation parameters β_L applies equally to the real, absorptive, and coulomb terms in the potential, i.e., $\beta_L^R = \beta_L^W = \beta_L^C$.

7) Besides the deformation parameters β_L, the values of the free adjustable parameters, N_R, W, r_I, and a_I, are chosen to fit the inelastic scattering cross section. These adjusted parameters are listed in Tables 4 and 8.
8) The procedure 7 is performed to study seven reactions, ^{58}Ni nuclei as an excited target at energies 288, 340, 480, and 699 MeV and ^{116}Sn nuclei as an excited target at 288, 340, and 480 MeV.

Table 6 Best-fit parameters of the optical potential obtained from analysis of α-particle scattering on ^{116}Sn and ^{208}Pb targets

Energy (MeV)	Potential	v (MeV)	N_R	$-J_R$ (MeV fm^3)	W_0 (MeV)	r_W (fm)	a_W (fm)	$-J_I$ (MeV fm^3)	χ^2	σ_R (mb)
288	$S1Y\,(R)$	33.7		148.5	6.90	1.636	0.840	78.20	4.0	3476
	$t\rho\rho\,(R)$		0.5	155.7	7.30	1.610	0.900	79.40	5.4	3474
340	$S1Y\,(R)$	33.4		146.5	7.36	2.200	0.760	88.30	5.8	3574
	$t\rho\rho\,(R)$		0.5	159.5	8.70	1.574	0.789	88.00	5.6	3336
480	$S1Y\,(R)$	16.2		71.4	41.0	1.090	0.671	142.0	8.0	2188
	$t\rho\rho\,(R)$		1.4	235.5	58.6	0.988	0.918	166.0	5.6	2438
288	$S1Y\,(R)$	35.5		152.4	7.90	1.574	0.760	68.00	5.4	4322
	$t\rho\rho\,(R)$		0.5	160.8	8.40	1.557	0.710	70.20	3.8	4245
340	$S1Y\,(R)$	34.5		148.4	8.30	1.583	0.757	73.00	9.4	4380
	tρρ (R)		1.0	291.6	37.9	1.121	0.629	120.3	9.0	2894
480	$S1Y\,(R)$	43.5		186.2	43.0	1.125	0.711	140.0	9.0	3061
	$t\rho\rho\,(R)$		1.5	241.6	45.4	1.070	0.931	133.3	8.0	3257
699	$S1Y\,(R)$	27.0		116.5	79.7	0.938	1.203	180.3	4.7	3536
	$t\rho\rho\,(R)$		1.0	213.4	108.3	0.858	1.250	199.4	3.6	3514

Table 7 Best-fit parameters of the optical potential considering the relativistic effect and second-order potential

Energy (MeV)	Potential	N_R	$-J_R$ (MeV fm^3)	W_0 (MeV)	r_W (fm)	a_W (fm)	$-J_I$ (MeV fm^3)	χ^2	σ_R (mb)
$\alpha+^{58}$Ni									
480	$t\rho\rho$ (R)	1.0	157.0	12.8	1.420	1.320	137.3	5.60	2675
	$t\rho\rho$ (R) (corr)	0.4	155.9	15.6	1.090	0.980	299.7	10.0	1531
	$t\rho\rho2$ (R)	1.0	304.8	18.8	1.260	1.970	263.0	9.40	2989
699	$t\rho\rho$ (R)	0.8	173.0	93.0	0.670	1.162	163.0	8.00	1651
	$t\rho\rho$ (R) (corr)	0.5	138.0	90.6	0.750	0.980	252.0	9.00	1424
	$t\rho\rho2$ (R)	0.7	226.9	96.9	0.642	1.231	203.0	7.40	1623
$\alpha+^{208}$Pb									
480	$t\rho\rho$ (R)	1.5	241.6	45.00	1.070	0.931	133.3	8.06	3257
	$t\rho\rho$ (R) (corr)	0.9	96.00	42.50	1.100	1.230	351.0	4.70	2935
	$t\rho\rho2$ (R)	1.4	102.5	36.50	1.610	0.896	499.5	6.80	3133
699	$t\rho\rho$ (R)	1.0	213.4	108.3	0.850	1.250	199.4	3.60	3536
	$t\rho\rho$ (R) (corr)	0.6	83.60	96.52	0.880	0.785	245.4	15.0	2748
	$t\rho\rho2$ (R)	0.8	445.0	86.30	1.110	1.193	398.0	3.00	3156

4 Results and Discussion

4.1 Elastic Scattering

The analysis of refractive α-particle elastic scattering on ^{58}Ni, ^{116}Sn, and ^{208}Pb nuclei are performed at energies 288, 340, 480, and 699 MeV. The real DF potentials are generated to analyze 11 sets of data. The best-fit parameters which are obtained in this analysis are listed in Tables 4, 5, 6, and 7. The corresponding real and imaginary volume integrals per nucleon (J_R and J_I) in MeV fm^3 and the total reaction cross sections σ_R in millibar are also listed in the tables. From Table 4, it is evident that the real and imaginary WS potentials are characterized by relatively small radius parameters ~0.95–1.1 fm for the real and imaginary parts. The real depths are clearly deeper than the imaginary ones. The real depth decreases with increasing energy and vice versa for the imaginary one.

We notice from Table 5 that the obtained values of the real *S1Y* strength (υ) for energies 288 and 340 MeV are consistent with those expected by Satchler [18] for HI reactions at intermediate energies. However, it is not the case at the other higher energies (480 and 699 MeV), where the obtained strengths are clearly larger than those suggested by Satchler

Table 8 Parameters obtained for transition optical potential from CC analysis

Energy	Potential	V_R (MeV)	N_R	W_I (MeV)	r_I (fm)	a_I (fm)	β_2 (fm)	δ_2^W (fm)
$\alpha+^{58}$Ni								
288	*S1Y* (R)	45.0		24.2	1.110	0.626	0.25	1.50
	$t\rho\rho$ (R)		0.9	24.2	1.070	0.597	0.25	1.46
340	*S1Y* (R)	45.0		26.8	1.031	0.796	0.25	1.40
	$t\rho\rho$ (R)		0.8	26.8	1.031	0.796	0.25	1.40
480	*S1Y* (R)	18.0		43.4	1.020	0.720	0.25	1.39
	$t\rho\rho$ (R)		1.1	43.4	1.130	0.721	0.25	1.54
699	*S1Y* (R)	30.0		42.3	0.989	0.750	0.25	1.35
	$t\rho\rho$ (R)		0.8	43.4	0.869	0.994	0.25	1.19
$\alpha+^{116}$Sn								
288	*S1Y* (R)	39.0		22.6	1.086	0.796	0.21	1.47
	$t\rho\rho$ (R)		0.7	22.6	1.086	0.796	0.21	1.47
340	*S1Y* (R)	38.7		25.6	0.991	0.995	0.21	1.35
	$t\rho\rho$ (R)		0.6	22.6	0.998	0.958	0.32	2.10
480	*S1Y* (R)	16.5		18.7	1.200	0.950	0.10	0.80
	$t\rho\rho$ (R)		0.5	25.7	1.060	1.000	0.15	1.03

[18], namely by about 35 % at 480 MeV and 37 % at 699 MeV. Another notice is that there is a clear energy dependence behavior for υ using the D2 density, where υ=40(1−0.07E) This result indicates that the *S1Y* effective interaction is

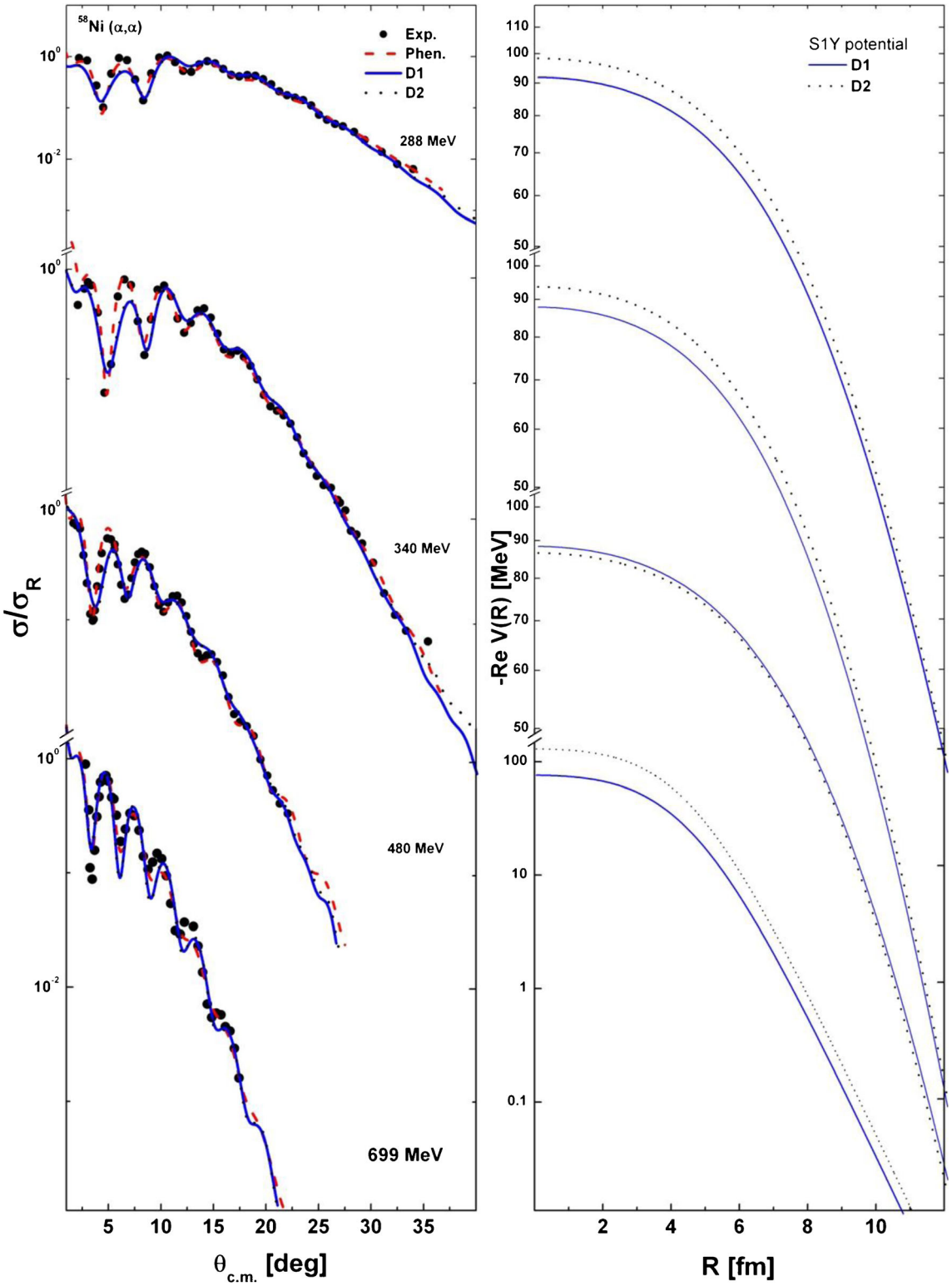

Fig. 1 Real DF optical potentials generated based upon the *S1Y* (*R*) effective *NN* interaction (*right panel*) folded with the Gaussian density (D1) [11] (*solid lines*) and Baye's density (D2) [27] (*dotted lines*). *Left panel* illustrates the corresponding DF potentials besides WS potential (*dashed lines*) calculations with angular distribution of the elastic α-particle scattering on ^{58}Ni at energies 288, 340, 480, and 699 MeV. Data are from ref. [14]

restricted over the energy range $E \leq 100$ MeV/nucleon. Another feature of the results shown in Table 5 is that the supplemented imaginary potentials at all the lower energies are shallower than those found from the complex phenomenological potentials as is shown in Table 4. Similar behavior is almost evident for the ^{116}Sn and ^{208}Pb targets as is listed in Table 6.

The renormalization factors required for the best fit of the $t\rho\rho$ potentials with data, as is listed in Tables 5, 6, and 7, are clearly lower than unity for the low energies and closer to unity at the higher considered energies. Therefore, one may conclude that the success of the $t\rho\rho$ potential is improved as energy increases ≥100 MeV/nucleon.

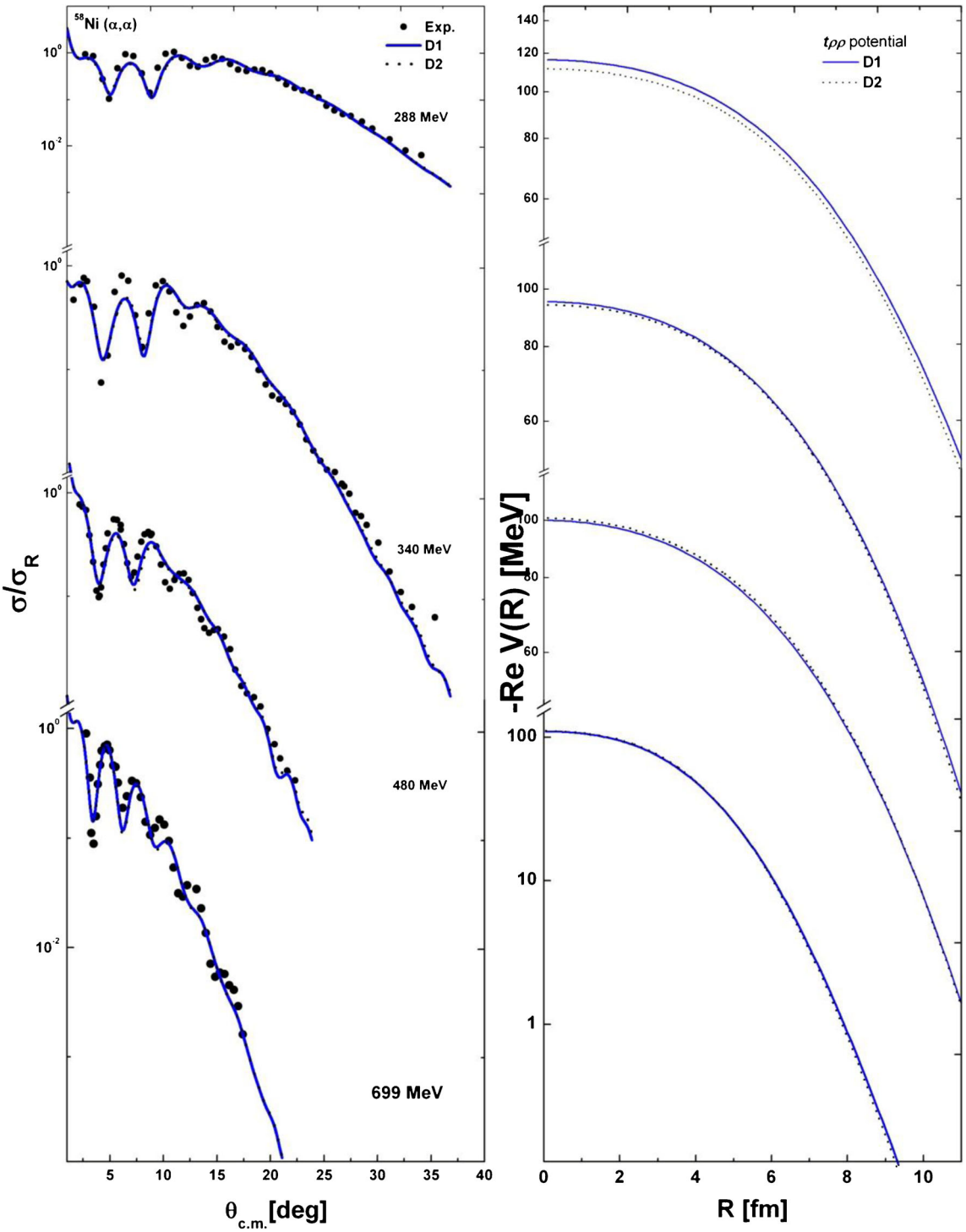

Fig. 2 Same as in Fig. 1 but for the $t\rho\rho$ (R) approximation

The right panels in Figs. 1 and 2 show a comparison between the normalized $S1Y(R)$ and $t\rho\rho(R)$ potentials derived using the α-particle density distributions D1 and D2 for ^{58}Ni target. It is quite noticeable that both potentials resemble each other all over the radial range. However, a slight divergence appeared near the origin.

Elastic scattering differential cross sections which are obtained for the considered reactions using the generated potentials are demonstrated in Figs. 1, 2, 3, 4, 5, and 6 in comparison with the corresponding experimental data. The obtained cross sections for α+^{58}Ni system are shown in the left panel in Figs. 1 and 2. It is clear that both D1 and D2 densities produced almost identical results all over the measured angular range using both the $S1Y$ and $t\rho\rho$ interactions. One may notice from Figs. 1 and 2 (and also considering the χ^2 values in Table 5) that $S1Y(R)$-based potentials produced better description of the data than $t\rho\rho(R)$ ones at the lower energies and vice versa at the highest energy, 699 MeV. This indicates that the success of the $t\rho\rho(R)$ interaction to describe the data is improved as energy increases. Similar conclusion may be extracted for the other targets regarding χ^2 values in Table 6 and Figs. 3 and 4.

For α+^{58}Ni and α+^{208}Pb reactions at energies 480 and 699 MeV, the $t\rho\rho$ approximation is corrected by Pauli blocking and higher-order multiple scattering effects. These potentials are denoted as ($t\rho\rho(R)$+corr). Also, the relativistic kinematics has been considered and referred as $t\rho\rho(R)$ potentials. The best-fit parameters are given in Table 7. As shown in Figs. 5 and 6, it is clear that the $S1Y(R)$ potentials give more successful description than $t\rho\rho(R)$ potentials, since the $t\rho\rho(R)$+corr and phenomenological potentials predict some stronger diffraction patterns than those observed in the experimental data at angular distributions $8 \leq \theta_{c.m.} \geq 17$ at energies E_a=288, 340, and 480 MeV.

The resulted volume integrals per interacting nucleon pair J_R from the $S1Y$ and $t\rho\rho$ potentials are shown in Tables 5, 6, and 7. The energy dependence of J_R for ^{58}Ni, ^{116}Sn, and ^{208}Pb targets is shown in Fig. 7. It is clear from this figure that the $S1Y$ and $t\rho\rho$ potentials reproduced almost consistent results for all considered energies. One may notice also that, in general, no clear behavior is identified for this energy dependence for all considered targets. The obtained target mass number dependence of J_R at the four considered energies for both $S1Y$ and $t\rho\rho$ potentials is illustrated in Fig. 8. It is easy to observe that the target mass number dependence of J_R at various energies has in general a linear behavior, where J_R slightly increases with increasing A_2. This result is clearly pronounced for $S1Y$ potential than that for $t\rho\rho$ one.

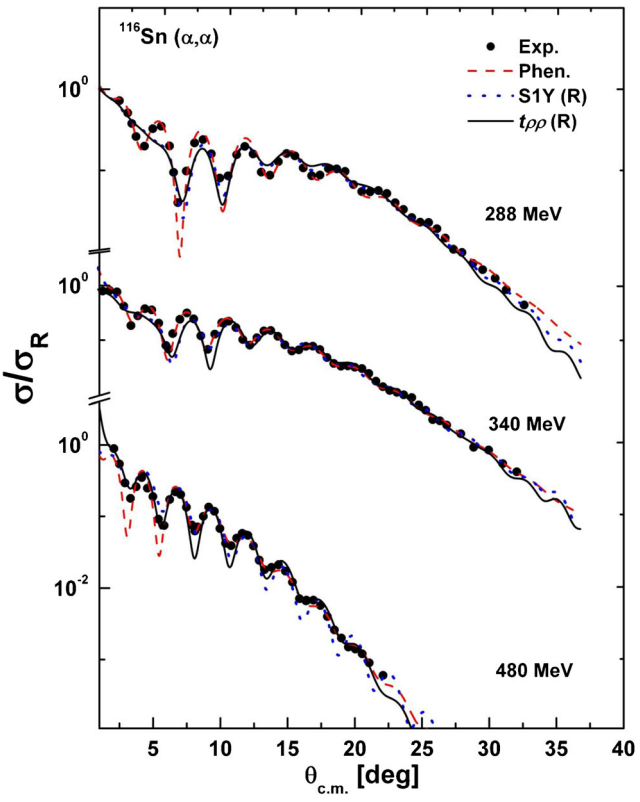

Fig. 3 Elastic α-particle scattering on ^{116}Sn at 288, 340, and 480 MeV, and the corresponding real DF potentials based upon $S1Y$ (R) effective NN interaction (*dotted lines*) and real $t\rho\rho$ (R) approximation (*solid lines*). Data are from ref. [14]

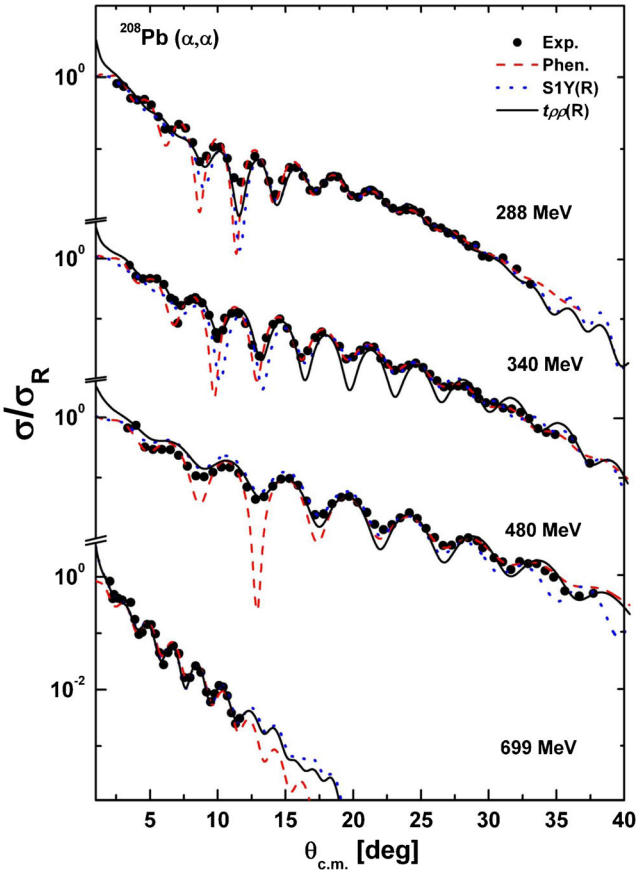

Fig. 4 Same as in Fig. 3 but for ^{208}Pb target

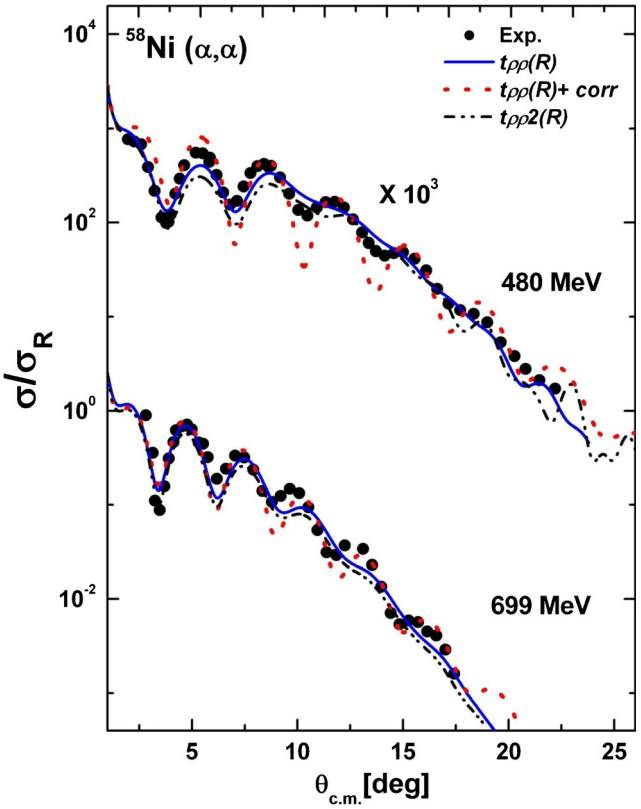

Fig. 5 The angular distribution of elastic α-particle scattering on ^{58}Ni at 480 and 699 MeV. The angular distributions of the data resulted by corresponding *tρρ* (R) calculations before (*solid lines*) and after (*short dotted lines*) adding the second-order resulted potential (*tρρ* (*R*)+corr). The relativistic effect resulted by *tρρ*2 (*R*) (*dashed dotted lines*)

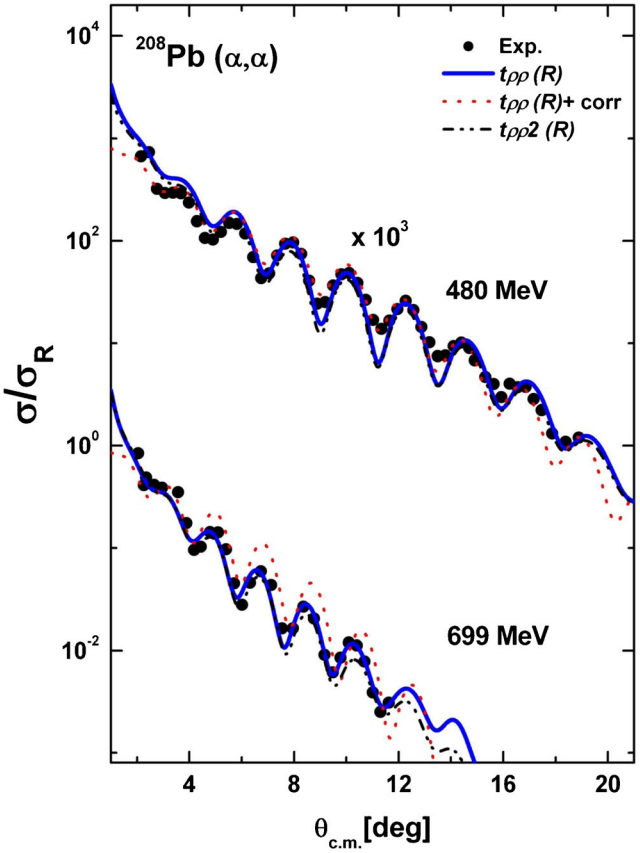

Fig. 6 Same as in Fig. 5 but for ^{208}Pb target

The calculated total reaction cross sections σ_R are listed in Tables 5, 6, and 7 and are plotted against $A_T^{1/3}$ at all considered energies, as is shown in Fig. 9. In general, the reaction cross section extracted using both *S1Y* and *tρρ* potentials increases with increasing A_T except at some points. This result is consistent with that previously found at intermediate energies [20]. On the other side, as shown in Tables 5, 6, and 7, a significant drop in σ_R at the highest considered energy (699 MeV) is observed. Similar result was previously [20] found during the analysis of this system using different potentials. This drop in σ_R at the highest energy (699 MeV) may be attributed to the corresponding drop of the *NN* total cross section around 200 MeV/nucleon.

4.2 Inelastic Scattering

The inelastic scattering for refractive α-nucleus on ^{58}Ni and ^{116}Sn as targets are analyzed for low-lying excited states (2^+) using the *S1Y* and *tρρ* effective interactions besides the phenomenological potentials. In the present studies, we analyze the angular distributions to the first excited state (2^+, 1.45 MeV) of ^{58}Ni target at the energies

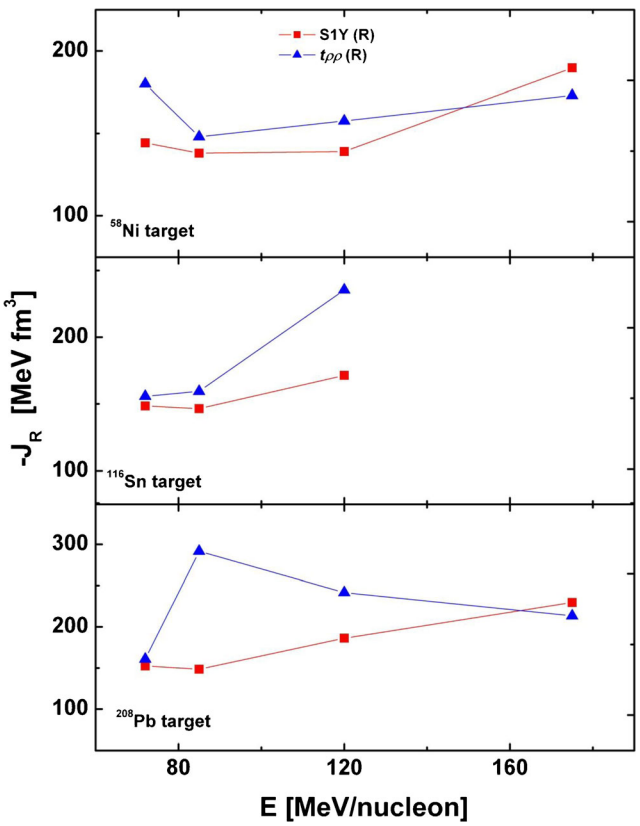

Fig. 7 Energy dependence of the real volume integrals of the obtained best-fit DF potentials for $_{58}$Ni, $_{116}$Sn, and $_{208}$Pb targets

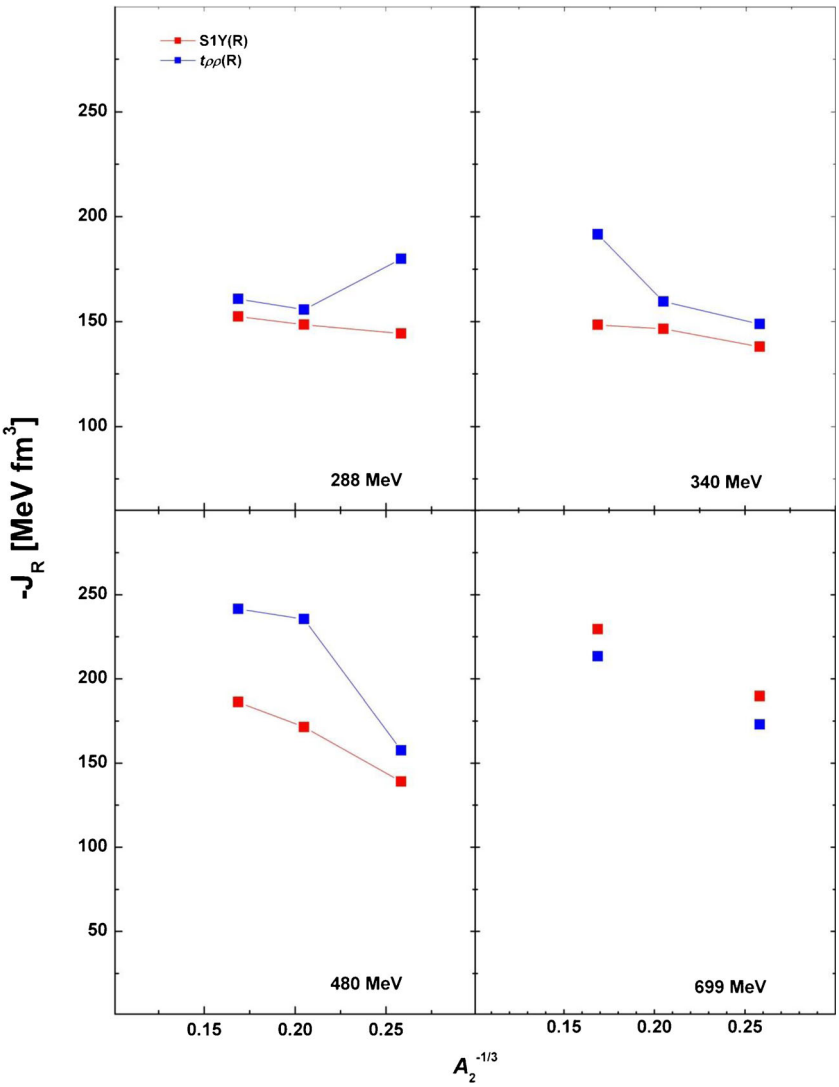

Fig. 8 The real volume integral per interacting nucleon pair J_R versus $A_T^{1/3}$ at 288, 340, 480, and 699 MeV

E_α=288, 340, 480, and 699 MeV and the first excited state (2^+, 1.28 MeV) of ^{116}Sn as target at energies E_α= 288, 340, and 480 MeV. The real DF transition potentials are used with CC calculations, while the WS potentials are used with DWBA calculations. In DWBA calculations of nuclear excitation, the form factor used is usually obtained by taking the derivative of the considered optical potential (elastic scattering optical potential). That is because it is expected the coupling effect decreases with increasing incident energy, which is understood as the result of a weaker nucleon-nucleon interaction and a shorter transit time of the projectile. Using the phenomenological WS parameters obtained from elastic scattering, DWBA calculations for excitation of low-lying states are carried out with DWUCK4 [34] code using collective form factors. The results of the DWBA calculations using these phenomenological potentials are summarized in Table 4. The results of these calculations reproduced the shape of the inelastic scattering distributions very well with deformation lengths δ_J obtained from

$$\delta_j = \beta_J R, \qquad R = r_0\left(A_P^{1/3} + A_T^{1/3}\right)$$

β_J is the nuclear deformation parameter, and R is nuclear radius. For a given excited state, the deformation parameter is obtained by effectively normalizing the experimental cross section to the DWBA or CC calculation,

$$\beta^2 = \frac{(d\sigma/d\Omega)_{\exp}}{(d\sigma/d\Omega)_{\mathrm{DWBA}}}$$

The deformation lengths obtained are given in Tables 4 and 8.

The calculations based on the CC using the semi-microscopic potentials are summarized in Table 8. The results of all of these calculations are demonstrated in Figs. 10 and 11

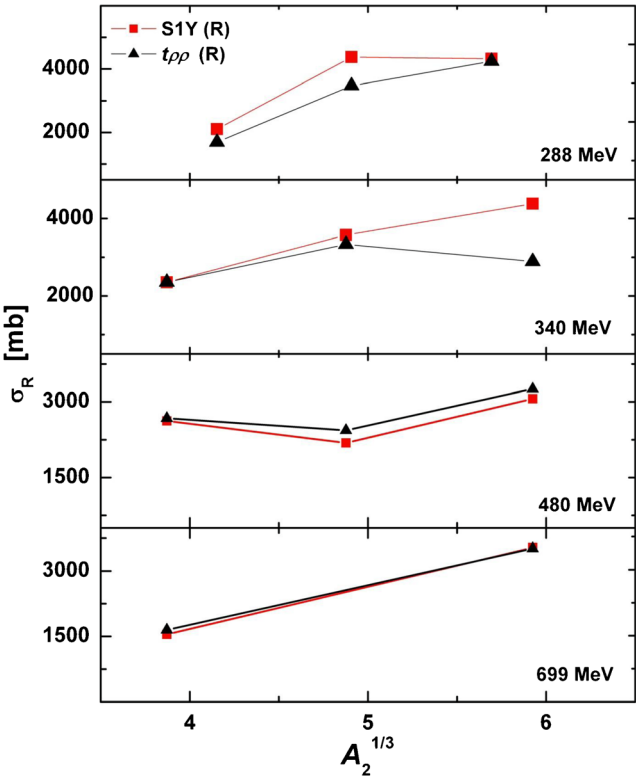

Fig. 9 The total reaction cross sections σ_R extracted from the calculations versus $A_T^{1/3}$ at energies 288, 340, 480, and 699 MeV

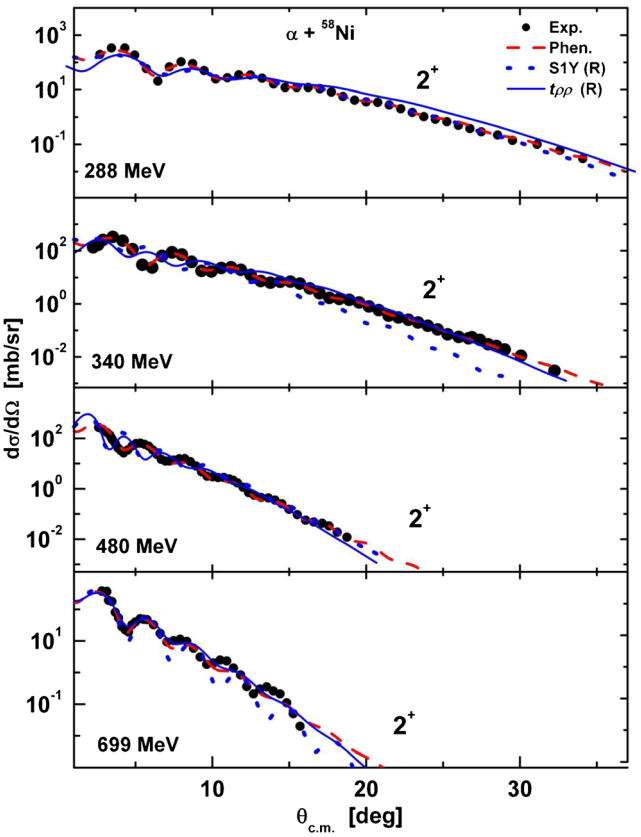

Fig. 10 Angular distribution of α-particle inelastic scattering on ^{58}Ni using the real *S1Y* (*R*) (*dotted lines*) and real *tρρ* (*R*) (*solid lines*) potentials besides the WS potentials (*dashed lines*)

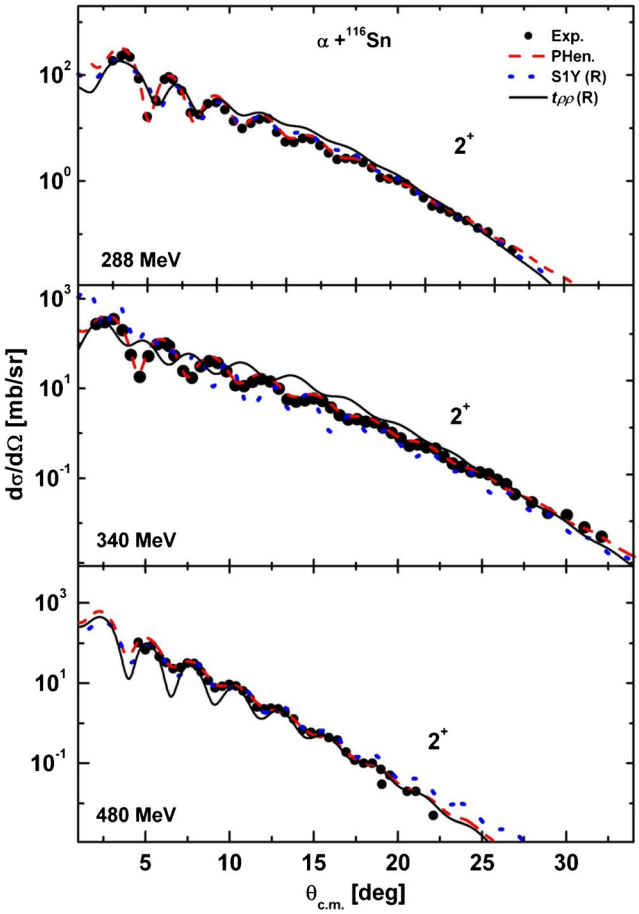

Fig. 11 Same as in Fig. 10 but for ^{116}Sn target

in comparison with experimental data. It is clear from these two figures that reasonable agreements with the data are obtained, at various ranges of energies, using the transition phenomenological potentials. We fixed a suitable value for deformation parameter β_2=0.14 for ^{58}Ni target and β_2=0.1 for ^{116}Sn target which is obtained from DWBA calculations using the transition phenomenological potentials. From Fig. 10, it is clear that the results based on the transition folded potentials derived from *S1Y* and *tρρ* effective interactions with the suggested densities are comparable with experimental data for ^{58}Ni target. It is quite noticeable that successful reproductions of the data are obtained at all energies for the two transition potentials. It is clear from values of the deformation lengths δ_2 in Table 8 that the deformation parameter β_2 at 0.25 for ^{58}Ni as excited target stays unchanged, while a slight change (0.32–0.15) for ^{116}Sn as an excited target is found.

We notice from the calculations that *S1Y* interaction has clear behavior and powerful ability to reproduce successful descriptions of the data much better than *tρρ* interaction. Nevertheless, the *tρρ* interaction gives agreement much better with data at high energy (699 MeV) than the *S1Y* effective interaction with potential strength N_R close to one.

5 Conclusion

The present work is devoted to analyze 13 sets of α-particle elastic and inelastic scattering data at the energies 288, 340, 480, and 699 MeV from ^{58}Ni and ^{116}Sn targets. The real DF optical potentials are generated to describe those reactions using the *S1Y* and the *tρρ* effective *NN* interactions. Both the *S1Y* interaction and *tρρ* approximation reasonably described the data. However, the latter provides much better agreement with the data at high energies. Successful descriptions of the data are obtained by these potentials all over the range of the angular distribution. The adjusted parameters are listed as computable with the parameters in earlier investigation [3, 6].

Finally, it is important to stress some main remarks for α-target scattering. First, the folding formalism presented here could also provide an accurate reference potential for the local α-core interaction in the description of the α-cluster structure in medium- and heavy-mass nuclei [36, 37]. We conclude that the DF real potentials with *S1Y* effective *NN* interaction and *tρρ* approximation have the same powerful ability in describing successfully elastic and inelastic scattering of α-particle at intermediate and high energies, up to 175 MeV/nucleon. Second, satisfactory agreement is obtained between our predictions and the data; also, the normalization factor N_R is close to unity when *tρρ* potentials are supplement with relativistic effects, while underestimations of the data with *tρρ* potentials are found at the considered energies.

References

1. A.M. Kobos, B.A. Brown, P.E. Hodgson, G.R. Satchler, A. Budzanowski, Nucl. Phys. **A384**, 65 (1982)
2. F. Petrovich, Nucl. Phys. **A251**, 143 (1975)
3. H.L. Clark, Y.W. Lui, D.H. Youngblood, Nucl. Phys. **A589**, 416 (1995)
4. T. Delbar et al., Phys. Rev. C **18**, 1237 (1978)
5. D.T. Khoa, Nucl. Phys. **A484**, 376 (1988)
6. B. Bonin, N. Alamanos, B. Berthier, G. Bruge, H. Faraggi, J.C. Lugol, W. Mittig, L. Parineau, A.I. Yavin, Nucl. Phys. **A445**, 381 (1985)
7. G. Satchler, W.G. Love, Phys. Rep. **55**, 183 (1979)
8. H. Abele, G. Staudt, Phys. Rev. C. **47**, 742 (1993)
9. H. Abele et al., Z. Phys. **A326**, 373 (1993)
10. M. El-AzabFarid, Z. M. M. Mahmoud and G. S. Hassan, Nucl. Phys. A691 (2001) 671; Phys. Rev C 64 (2001) 014310
11. M. El-AzabFarid, Phys. Rev C 65 (2002) 067303; 74 (2006) 064616
12. M.A. Hassanain et al., Phys. Rev. C. **87**, 064606 (2013)
13. K. O. Behairy, Assuit University J. Phys. 2013
14. W.G. Love, M.A. Franey, Phys. Rev. C. **14**, 1073 (1981)
15. M.A. Franey, W.G. Love, Phys. Rev. C. **31**, 488 (1985)
16. L. Ray, Phys. Rev. C. **20**, 1857 (1979)
17. M.S. Hussein, R.A. Rego, C.A. Bertulani, Phys. Rep. **201**, 279 (1991)
18. G.R. Satchler, Nucl. Phys. **A579**, 421 (1994)
19. P.D. Hodgson, *Nuclear reactions and nuclear structure* (Press Oxford, Clarendon, 1971)
20. A. Nadasen, P. Schwandt, P.P. Singh, W.W. Jacobs, A.D. Bacher, P.T. Debevec, M.D. Kaitchuck, J.T. Meek, Phys. Rev. C **23**, 1023 (1981)
21. M. K. Metha and J. J. Schmidt, Applied Nuclear Theory and Nuclear TechnologyApplications, (Trieste, 1988)
22. M. El-AzabFarid, G.R. Satchler, Phys. Lett. **B146**, 389 (1984)
23. G.R. Satchler, Nucl. Phys. **A540**, 533 (1992)
24. M. El-AzabFarid, Phys. Rev. C. **74**, 064616 (2006)
25. D. Baye, L. Desorgher, D. Guillain, D. Herschkowitz, Phys. Rev. C. **54**, 2563 (1996)
26. M. Jaminon, C. Mahaux, Phys. Rev. C. **34**, 2097 (1986)
27. Y. Sakuragi, Phys. Lett. **B220**, 22 (1989)
28. P. Shukla, Phys. Rev. C. **67**, 054607 (2003)
29. L.C. Chamon et al., Phys. Rev. C **66**, 014610 (2002)
30. E. Boridy, H. Feshbach, Ann. Phys. (NY) **109**, 468 (1977)
31. N. M. Clarke, (1994) (unpublished)
32. D.F. Jackson, *Nuclear reactions* (Science Paperback, London, 1975)
33. G.R. Satchler, *Direct nuclear reactions* (Oxford Univ. Press, Oxford, 1983)
34. P. D. Kunz, 1993 (private communication)
35. P. D. Kunz, Computer Program, (1984) (unpublished)
36. D.T. Khoa, Phys. Rev. C. **63**, 034007 (2001)
37. M. Avrigeanu, W. von Oertzan, H.G. Boheln, Nucl. Phys. **A723**, 104 (2003)